Nucleic Acids Research, 2024, **52**, 816–830
https://doi.org/10.1093/nar/gkad1149
Advance access publication date: 4 December 2023
Molecular Biology

Dynamic action of an intrinsically disordered protein in DNA compaction that induces mycobacterial dormancy

Akihito Nishiyama [1,*], Masahiro Shimizu [2,3], Tomoyuki Narita [2], Noriyuki Kodera [2], Yuriko Ozeki [1], Akira Yokoyama [1,4], Kouta Mayanagi [5], Takehiro Yamaguchi [1,6], Mariko Hakamata [1,7], Amina Kaboso Shaban [1], Yoshitaka Tateishi [1], Kosuke Ito [8] and Sohkichi Matsumoto [1,9,10,*]

[1]Department of Bacteriology, Niigata University School of Medicine, 1-757 Asahimachi-dori, Chuo-ku, Niigata 951-8510, Japan
[2]Nano Life Science Institute, Kanazawa University, Kakumamachi, Kanazawa, Ishikawa 920-1192, Japan
[3]Division of Quantum Beam Material Science, Institute for Integrated Radiation and Nuclear Science, Kyoto University, 2 Asashiro-Nishi, Kumatori, Sennan-gun, Osaka 590-0494, Japan
[4]Department of Respiratory Medicine, Graduate School of Medicine, The University of Tokyo, 7-3-1 Hongo, Bunkyo-ku, Tokyo 113-8655, Japan
[5]Medical Institute of Bioregulation, Kyushu University, 3-1-1 Maidashi, Higashi-ku, Fukuoka 812-8582, Japan
[6]Department of Pharmacology, Osaka Metropolitan University Graduate School of Medicine, 1-4-3 Asahimachi, Abeno-ku, Osaka 545-8585, Japan
[7]Department of Respiratory Medicine and Infectious Disease, Niigata University School of Medicine, 1-757 Asahimachi-dori, Chuo-ku, Niigata 951-8510, Japan
[8]Graduate School of Science and Technology, Niigata University, 2-8050 Ikarashi, Nishi-ku, Niigata 950-2181, Japan
[9]Laboratory of Tuberculosis, Institute of Tropical Disease, Universitas Airlangga, Kampus C Jl. Mulyorejo, Surabaya, East Java 60115, Indonesia
[10]Division of Research Aids, Hokkaido University Institute for Vaccine Research & Development, Kita 20, Nishi 10, Kita-ku, Sapporo, 001-0020, Japan

[*]To whom correspondence should be addressed. Tel: +81 25 227 2050; Fax: +81 25 227 0764; Email: anishi@med.niigata-u.ac.jp.
Correspondence may also be addressed to Sohkichi Matsumoto. Tel: +81 25 227 2050; Fax: +81 25 227 0764; Email: sohkichi@med.niigata-u.ac.jp
Present addresses:
Kouta Mayanagi, Faculty of Pharmaceutical Sciences, Kyushu University, 3-1-1 Maidashi, Higashi-ku, Fukuoka 812-8582, Japan.
Takehiro Yamaguchi, Department of Bacteriology I, National Institute of Infectious Diseases, 1-23-1 Toyama, Shinjuku-ku, Tokyo 162-8640, Japan.

Abstract

Mycobacteria are the major human pathogens with the capacity to become dormant persisters. Mycobacterial DNA-binding protein 1 (MDP1), an abundant histone-like protein in dormant mycobacteria, induces dormancy phenotypes, e.g. chromosome compaction and growth suppression. For these functions, the polycationic intrinsically disordered region (IDR) is essential. However, the disordered property of IDR stands in the way of clarifying the molecular mechanism. Here we clarified the molecular and structural mechanism of DNA compaction by MDP1. Using high-speed atomic force microscopy, we observed that monomeric MDP1 bundles two adjacent DNA duplexes side-by-side via IDR. Combined with coarse-grained molecular dynamics simulation, we revealed the novel dynamic DNA cross-linking model of MDP1 in which a stretched IDR cross-links two DNA duplexes like double-sided tape. IDR is able to hijack HU function, resulting in the induction of strong mycobacterial growth arrest. This IDR-mediated reversible DNA cross-linking is a reasonable model for MDP1 suppression of the genomic function in the resuscitable non-replicating dormant mycobacteria.

Received: March 8, 2023. **Revised:** October 17, 2023. **Editorial Decision:** November 13, 2023. **Accepted:** November 23, 2023

Graphical abstract

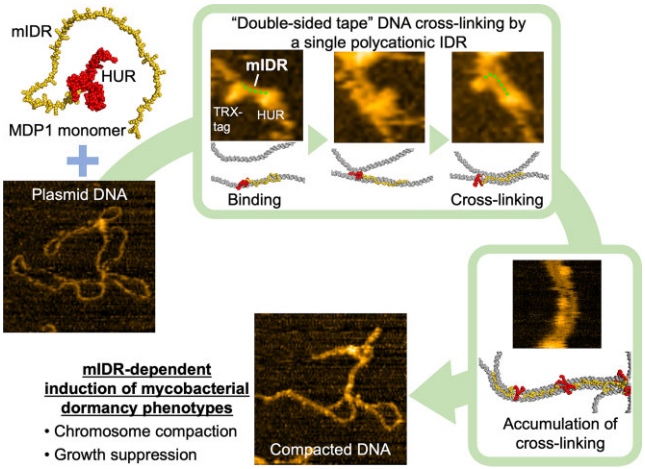

Introduction

Cells age and die after halting replication. However, parts of cellular organisms can enter into a non-replicating dormant phase resulting in a long life span. Dormancy is useful to survive in stringent conditions such as hypoxia, starvation or other environmental stresses. Therefore, dormant bacteria frequently establish chronic infections and cause intractable diseases (1). In such stationary, dormant or stress-exposed bacteria, chromosome compaction has been frequently observed. Nucleoid-associated proteins are involved in such chromosome compaction (2–7).

Mycobacteria are the major human pathogens that are prone to become dormant persisters. For example, dormant *Mycobacterium tuberculosis* var. *tuberculosis* [*Mtb*, formerly known as *M. tuberculosis* (8)] persistently infects a quarter of the human population. Approximately 5–10% of latent infections eventually become active tuberculosis by reactivation, resulting in 1.5 million deaths annually (9). Mycobacteria including *Mtb* express a unique histone-like protein, mycobacterial DNA-binding protein 1 (MDP1) (Figure 1A), whose expression is elevated at stationary and dormant phases (2,10,11). We have reported that MDP1 induces dormant phenotypes, e.g. chromosome compaction, growth suppression and isoniazid tolerance (2,11,12).

MDP1 is an ortholog of histone-like protein HU [initially reported as a heat-stable DNA-binding protein in *Escherichia coli* strain U93 (13)], which is a conserved protein among eubacteria (10,12,14). In general, HU is an ∼90 amino acid polypeptide and revealed similar dimer structures (e.g. HUαα and HUαβ in *E. coli*) (14–17). HU dimer embraces and bends double-stranded DNA (dsDNA) by β-arms stretched from each protomer (15). The MDP1 N-terminal region (residues 1–99) is highly conserved among mycobacterial species and revealed similarities to HU proteins (Figure 1A). X-ray crystallography of MDP1 showed a homodimer structure of the N-terminal region which is similar to that of an HU homodimer (18). We thus call it the HU-like region (HUR; Figure 1A).

Interestingly, following the HUR, MDP1 has a long and unique (≥100 residue) C-terminal tail which is absent in general HUs (Figure 1A) (2,14). The MDP1 C-terminal tail has similar characteristics to the C-terminal intrinsically disordered region (IDR) of eukaryotic histone H1 (C-IDR$_{H1}$) which is rich in Lys and short sequence repeats (PAKK), lacks a typical secondary structure except for a few α-helices (2,14,19), and is invisible in X-ray crystal structure (18) (Figure 1A; Supplementay Figure S1A, B). We thus indicated that this C-terminal tail is an IDR of MDP1 (mIDR) (2). Importantly, we have shown that MDP1 activities, such as, chromosome compaction, growth suppression and isoniazid tolerance, are dependent on mIDR (2). Thus, MDP1 functions are likely to be mediated by mIDR.

IDRs do not follow the traditional doctrine in which protein function is determined by its three-dimensional (3D) structure. This is because IDRs alone do not exhibit a typical secondary and higher structure due to low sequence complexity and amino acid composition bias (20,21). IDRs are abundant in eukaryotic proteins (21–24), especially in intranuclear proteins (47% of total residues) and transcription factors (63% of total residues) (25,26). Their functions have been extensively studied in eukaryotic proteins. For instance, C-IDR$_{H1}$ of histone H1 regulates chromatin condensation and epigenetic inheritance (27).

On the other hand, the role of IDRs in bacterial proteins is largely unknown. IDR-containing bacterial proteins are less common than in eukaryotes. For instance, IDRs longer than 50 residues are found in only 1.6% of the bacterial proteins (21). Thus, long IDRs are rare among bacterial proteins including bacterial histone-like proteins (26) and it can be said that MDP1 is a unique intrinsically disordered protein with a long histone tail-like IDR among bacteria. The detailed molecular action of mIDR in MDP1 functions has so far not been elucidated due to its distinctively disordered nature.

High-speed atomic force microscopy (HS-AFM) is a technique that enables real-time observation of the dynamics of intact macromolecules (e.g. DNA, RNA and proteins) in aqueous solution (28–31). HS-AFM time-lapse imaging has been used to visualize molecular activities such as myosin V walking along the actin fiber (32), the dynamic DNA cleavage processes by Cas9 (29) and the dynamics of nucleosome structures (30,31). Kodera *et al.* have also shown that HS-AFM imaging and time resolution are sufficient to elucidate the dynamic actions and disorder-to-order shift of a single IDR using polyglutamine tract-binding protein-1 (PQBP-1) and

autophagy proteins (Atg1 and Atg13) (33). Thus HS-AFM is useful to determine the dynamic action of IDRs.

The combination of experimental structure data and molecular dynamic (MD) simulation has also been used to predict structures and dynamics of molecules including IDRs. Coarse-grained molecular dynamics (CGMD) simulation is an MD simulation in which each substructure (e.g. amino acid residue; base and deoxyribose of a nucleotide) of a macromolecule is represented as a single particle (34,35). It is a tool to predict the dynamic structural model of large macromolecules such as proteins (including IDRs), nucleic acids and their complexes, compared with atomistic MD simulation in terms of saving calculation steps and time (36,37).

In this study, we employed HS-AFM coupled with computational CGMD simulation, and revealed details of the dynamic molecular action of mIDR during DNA compaction by MDP1. Here, we show a novel dynamic model of DNA compaction that is a reasonable mechanism to suppress genomic function in resuscitable dormant mycobacteria.

Materials and methods

Bacterial strains, culture media and general reagents:

An *mdp1*$_{Msm}$-defficient strain of *Mycolicibacterium smegmatis* (*Msm*) mc^2_155 (*Msm* Δ*mdp1*), which was formerly known as *Mycobacterium smegmatis* (8), was kindly provided by Dr John L. Dahl (University of Minnesota Duluth) (38). *Escherichia coli* DH5α strain was used for all gene manipulation in this study. Clear coli BL21(DE3) was purchased from Lucigen (Madison, WI, USA). All *Msm* strains were grown in Middlebrook 7H9 broth (BD, Franklin Lakes, NJ, USA) supplemented with 0.2% (v/v) glycerol, 0.05% (v/v) Tween-80 (MP Biomedicals, Santa Ana, CA, USA) and 10% ADC enrichment [5% bovine serum albumin (FUJIFILM Wako Pure Chemical Corporation, Osaka, Japan), 0.81% NaCl and 2% D-glucose] (7H9-ADC broth) or on Middlebrook 7H10 agar (BD) supplemented with 0.5% (v/v) glycerol and 10% OADC enrichment [ADC enrichment supplemented with 0.06% (v/v) oleic acid] (7H10-OADC agar) for transformation and analysis, and in Mueller–Hinton II Broth, Cation-Adjusted, (MHB, BD) supplemented with 0.05% (v/v) Tween-80 (MHB/Tw80) for protein purification. All *E. coli* strains were cultured in LB broth or on LB agar (both from Sigma-Aldrich, St. Louis, MO, USA). Appropriate antibiotics were also added to the media to maintain specific genotypes of each strain. Hygromycin B (Hyg), kanamycin (Km), ampicillin (Amp), acetamide (Ace) and isopropyl β-D-thiogalactopyranoside (IPTG) were purchased from FUJIFILM Wako Pure Chemical Corporation.

Other methods

Other experimental procedures are described in the Supplementary data.

Results

MDP1 compacts DNA duplexes via side-by-side DNA bundling

We first examined if HS-AFM could track MDP1–DNA interaction. MDP1 binds to DNA with low sequence specificity; thus, in this study, we used a 4.5 kb plasmid [pSO246, Supplementary Table S2 (39) and Supplementary Figure S1C, supercoiled] as a binding target for MDP1. We used MDP1 (MDP1$_{Msm}$) purified from *Msm*. By gel retardation assay, MDP1$_{Msm}$ bound to the pSO246 plasmid both in PBS(–) and HS-AFM imaging buffer (10 mM Tris–HCl pH 7.5, 20 mM NaCl, 60 mM KCl) with similar DNA affinity (Figure 1B; Supplementary Figure S1D). We performed time-lapse imaging of the DNA/MDP1$_{Msm}$ complex formation by HS-AFM. pSO246 plasmids (supercoiled) were attached to the mica stage in protein-free buffer (Figure 1C, no protein, see the Supplementary data). After addition of MDP1$_{Msm}$, small globules appeared on dsDNAs and then two adjacent dsDNAs were cross-linked side-by-side, which consequently induced DNA compaction (Supplementary Video S1; Figure 1C, +MDP1$_{Msm}$). We also observed similar DNA strand bundling when *Mtb* MDP1 (MDP1$_{Mtb}$) was added (Figure 1C, +MDP1$_{Mtb}$). We were able to quantify DNA compaction by monitoring changes in areas enclosed by each plasmid (Figure 1D). Taken together, the revealed AFM structure of the DNA/MDP1 complex is different from the previously reported DNA complex with general HU that exhibits DNA bending, an uncompacted rigid DNA strand or more relaxed loop structures (40–42). Rather, the filamentous DNA bundling structure by MDP1 was similar to an AFM image of a DNA complex with histone-like nucleoid structuring protein (H-NS), which does not possess a histone-like IDR (40,43).

On the other hand, compaction of a relatively large open region was less frequent (Figure 1E, indicated by arrows), suggesting that the proximity of the DNA strands determines the efficacy of DNA compaction by MDP1. To test this hypothesis, we prepared two additional forms of plasmids [relaxed (nicked open ring) and linear forms, Supplementary Figure S1C]. As we reported previously using pBSKS plasmid (10), MDP1$_{Msm}$ affinity for the supercoiled pSO246 was slightly higher than those for other forms (Supplementary Figure S1E, F). Under HS-AFM using these plasmid preparations, MDP1$_{Msm}$ bundled part of the relaxed and linear plasmids where the strands were closely located (Figure 1F; Supplementary Video S1e, f). However, the compaction of these plasmids was insignificant (Figure 1G). Thus, the proximity of dsDNAs seems crucial for efficient DNA compaction by MDP1.

mIDR plays a crucial role in MDP1-induced DNA compaction

We previously revealed that mIDR is essential for MDP1 to induce dormant phenotypes in mycobacteria (2). Therefore, we next investigated the role of each MDP1$_{Msm}$ N-terminal HUR (HUR$_{Msm}$, 1–99 residue region) and C-terminal mIDR (mIDR$_{Msm}$, 100–208 residue region) (Figure 2A, B) in DNA compaction *in vitro*.

We first assessed the affinities of HUR$_{Msm}$ and mIDR$_{Msm}$ (44,45) for the synthesized 70 bp dsDNA of *the Msm furA-katG* promoter region [$P_{furA\text{-}katG}$ (Supplementary Table S1)], a target of isoniazid tolerance by MDP1 (11), using a gel retardation assay (Supplementary Figure S2A, B) and biolayer interferometry quantification assay (Supplementary Table S3), and with the supercoiled plasmid (employed in Figure 1B), using a gel retardation assay (Figure 2C; Supplementary Figure S2C). mIDR$_{Msm}$ showed DNA affinity for both the 70 bp $P_{furA\text{-}katG}$ fragment (Supplementary Figure S2A, B; Supplementary Table S3) and the supercoiled plasmid

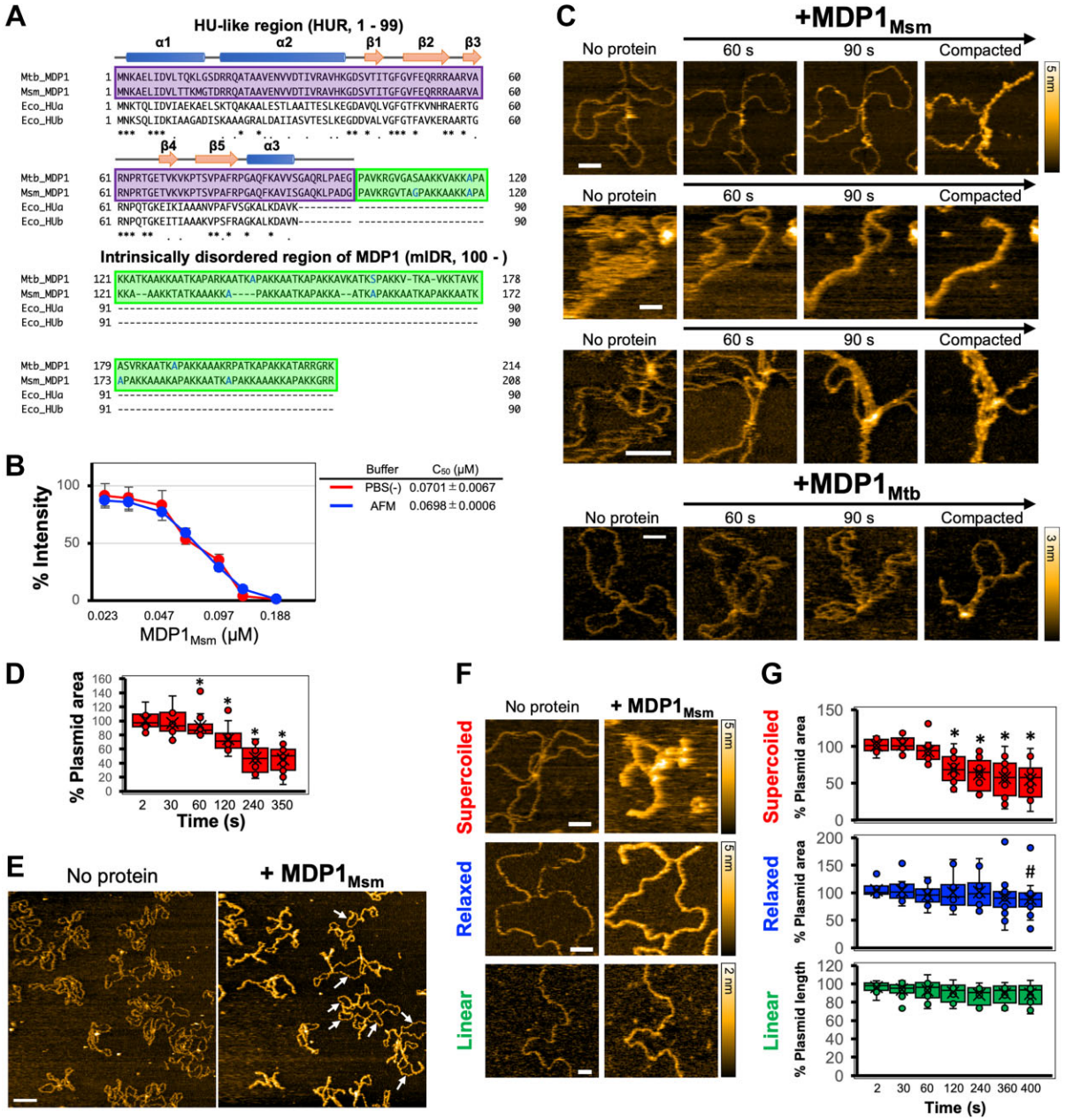

Figure 1. MDP1 induced DNA compaction via side-by-side DNA bundling. (**A**) Amino acid sequences of $MDP1_{Msm}$, $MDP1_{Mtb}$, *E. coli* HUα and HUβ. Secondary structures of $MDP1_{Mtb}$ HUR_{Mtb} (18) are presented as α-helices (tubes) and β-strands (arrows) at the top of the alignment. Purple and green boxes indicate MDP1 HUR and mIDR, respectively (2,18). Aligned sequences are as follows: Mtb_MDP1, *Mtb* H37Rv $MDP1_{Mtb}$ (AL123456, Rv2986c); Msm_MDP1, *Msm* mc^2_155 $MDP1_{Msm}$ (CP000480, MSMEG_2389); Eco_HUa, *E. coli* K-12 MG1655 HUα (U00096, b4000); and Eco_HUb, *E. coli* K-12 MG1655 HUβ (b0440). (**B**) Affinity of $MDP1_{Msm}$ for supercoiled pSO246 (gel retardation assay) in PBS(–) or HS-AFM imaging buffer (AFM). Representative gels are shown in Supplementary Figure S1D. Band intensity of the plasmid migrated at the position indicated by arrows in Supplementary Figure S1D was measured using Image J Fiji and plotted (mean ± SD, $n = 3$). The protein concentration which induced 50% DNA retardation (C_{50}) was calculated from fitted curves of triplicate gels and indicated in the panel. The difference was not significant. (**C**) HS-AFM time-lapse imaging of $MDP1_{Msm}$- and $MDP1_{Mtb}$-induced morphological changes of 4.5 kb plasmids. A plasmid-bound mica stage was set-up, followed by protein addition to the buffer chamber. Images were then taken [5 frames per second (fps)]. Bars, 60 nm. Corresponding movies are presented in Supplementary Video S1a–c. (**D**) Plasmid compaction. Time-lapse images were captured by HS-AFM at 0.5 fps (1500 nm × 1500 nm). Plasmid compaction was followed by measuring the areas enclosed by individual plasmids (Image J Fiji). The area of protein-free plasmid was considered as 100% and the % plasmid area at each time point was plotted ($n = 18$). $^{*}P < 0.05$ compared with the data at 2 s (Kruskal–Wallis test and Mann–Whitney test). (**E**) Overview of the plasmids before and after compaction by $MDP1_{Msm}$ (0.5 fps). Arrows, circular regions not compacted by $MDP1_{Msm}$. Bar, 150 nm. (**F**) Comparison of $MDP1_{Msm}$-induced morphological changes of the supercoiled, relaxed and linear plasmids by HS-AFM (5 fps). Left, protein-free; right, incubated with $MDP1_{Msm}$. Bars, 60 nm. Corresponding movies are presented in Supplementary Video S1d–f. (**G**) Compaction of supercoiled, relaxed and linear plasmids was quantified as described in (C) ($n \geq 13$). $^{*}P < 0.05$ compared with the data at 2 s; $^{\#}P < 0.05$ compared with the supercoiled plasmid (Kruskal–Wallis test and Mann–Whitney test). See also Supplementary Figure S1 and Supplementary Video S1.

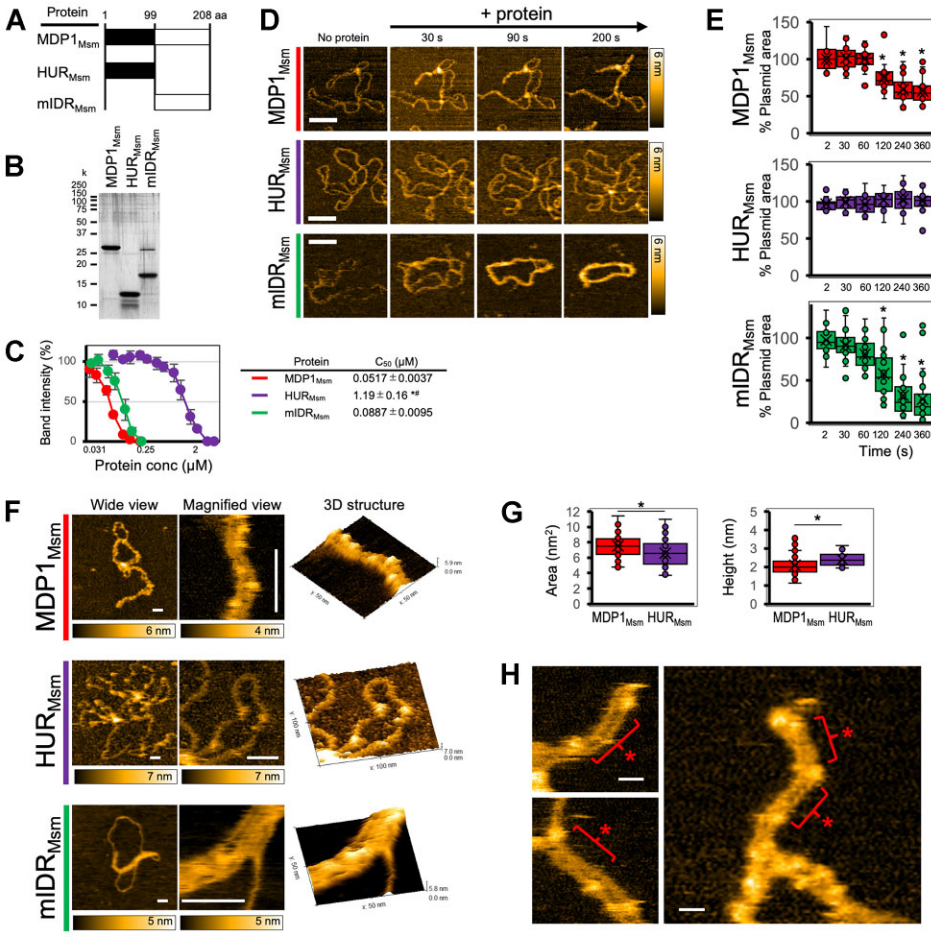

Figure 2. mIDR plays a crucial role in MDP1-induced DNA compaction. (A and B) Schematic representation (**A**) and sodium dodecylsulfate–polyacrylamide gel electrophoresis (SDS–PAGE) (**B**) of $MDP1_{Msm}$, HUR_{Msm} and $mIDR_{Msm}$. (**C**) Affinity of $MDP1_{Msm}$, HUR_{Msm} and $mIDR_{Msm}$ for the supercoiled plasmid (gel retardation assay). Representative gels are shown in Supplementary Figure S2C. Band intensity (mean ± SD, $n = 3$) and C_{50} (mean ± SD, $n = 3$) were calculated as described in Figure 1B. $^{*}P < 0.05$ compared with $MDP1_{Msm}$ and $^{\#}P < 0.05$ compared with $mIDR_{Msm}$ [analysis of variance (ANOVA)]. (**D**) HS-AFM time-lapse imaging of plasmid morphological changes caused by $MDP1_{Msm}$, HUR_{Msm} or $mIDR_{Msm}$ performed as described in Figure 1C (5 fps). Bars, 100 nm. Corresponding movies are presented in Supplementary Video S2. (**E**) Plasmid compaction was quantified as described in Figure 1D ($n \geq 18$). $^{*}P < 0.05$ compared with data at 2 s. $^{\#}P < 0.05$ compared with $MDP1_{Msm}$ and $^{\dagger}P < 0.05$ compared with $mIDR_{Msm}$ (Kruskal–Wallis test and Mann–Whitney test). (**F**) Detailed images of DNA/protein complexes, captured by HS-AFM (5 fps). Bars, 30 nm. 3D structures of DNA/protein complexes were generated using Gwyddion (http://www.gwyddion.net). (**G**) The area and height of the globules detected on DNA/$MDP1_{Msm}$ and DNA/HUR_{Msm} complexes were measured using Image J Fiji and Kodec, respectively. $MDP1_{Msm}$, median area 7.50 nm^2, median height 2.00 nm; HUR_{Msm}, median area 6.55 nm^2, median height, 2.36 nm. $^{*}P < 0.05$ (Student *t*-test for area and Mann–Whitney test for height). (**H**) Sporadic localization of $MDP1_{Msm}$ globules on DNA/$MDP1_{Msm}$ complexes. *Cross-linked DNA regions between $MDP1_{Msm}$ globules. Bars, 10 nm. See also Supplementary Figure S2; Supplementary Videos S2 and S3; and Supplementary Table S3.

(Figure 2C; Supplementary Figure S2C), comparable with that of intact $MDP1_{Msm}$. HUR_{Msm} also bound to these target DNAs. However, HUR_{Msm} required ≥10-fold protein concentrations to induce 50% DNA retardation (C_{50}), compared with $MDP1_{Msm}$ and $mIDR_{Msm}$ in the gel retardation assay (Figure 2C; Supplementary Figure S2), and exhibited a >2000-fold higher dissociation constant (*Kd*), compared with $MDP1_{Msm}$ and $mIDR_{Msm}$ in the biolayer interferometry quantification assay (Supplementary Table S3). Thus, major DNA affinity of MDP1 is derived from mIDR.

Using HS-AFM, we next monitored the plasmid morphological changes induced by HUR_{Msm} and $mIDR_{Msm}$. Corresponding to low DNA affinity, the DNA association of HUR_{Msm} globules was less frequent and more transient than that of intact $MDP1_{Msm}$ globules (Figure 2D HUR_{Msm}; Supplementary Video S2b). In addition, HUR_{Msm} hardly exhibited compact plasmids (Figure 2E, HUR_{Msm}). In contrast, $mIDR_{Msm}$ alone compacted plasmids more than intact $MDP1_{Msm}$ (Figure 2D, E, $mIDR_{Msm}$; Supplementary Video S2c). Thus, mIDR is responsible for DNA compaction by MDP1.

In detail, similar globules were observed on DNA after $MDP1_{Msm}$ or HUR_{Msm} addition (Figure 2F, G, $MDP1_{Msm}$, median area 7.50 nm^2, median height 2.00 nm; HUR_{Msm}, median area 6.55 nm^2, median height, 2.36 nm). Such globules were not seen upon $mIDR_{Msm}$ addition. Thus, each single globule on DNA/$MDP1_{Msm}$ complexes is ascribed to HUR_{Msm} of an $MDP1_{Msm}$ molecule. The DNA/$MDP1_{Msm}$ complex remained relatively flexible even after DNA compaction occurred. The globules were allowed to move on the compacted dsDNAs, although association of the globules with dsDNAs was relatively stable (Supplementary Video S3a–c). Such single $MDP1_{Msm}$ globules were frequently found on either of the bundled dsDNAs, not paired (Figure 2F, $MDP1_{Msm}$), suggest-

ing that a single $MDP1_{Msm}$ molecule can cross-link two dsDNAs.

The dsDNAs were cross-linked not only at the binding sites of the globules but also between the globules (Figure 2H, *), suggesting that $mIDR_{Msm}$ extends from the HUR_{Msm} globules to cross-link dsDNAs. In the absence of HUR_{Msm}, $mIDR_{Msm}$ appeared to form amorphous broad bands that were randomly located between or across dsDNAs (Figure 2F, $mIDR_{Msm}$). $mIDR_{Msm}$ is indistinguishable from other structures by HS-AFM analysis (Figure 2F, H). Hence, we could not deduce the molecular action of mIDR during DNA compaction by MDP1 from these HS-AFM data.

mIDR bands or tapes two dsDNAs together by the monomer form

In order to investigate mIDR action in the process of DNA compaction, we fused thioredoxin (TRX), which is visible by HS-AFM (33), to the $MDP1_{Msm}$ C-terminus and designated it as MDP1-TRX (Figure 3A). We confirmed that MDP1-TRX has comparable DNA affinity (Figure 3B, C; Supplementary Table S3). MDP1-TRX also compacted plasmid DNA, although it took longer (Supplementary Figure S3A) and was relatively less efficient than $MDP1_{Msm}$ (Supplementary Figure S3B). This could in part be caused by steric hindrance of TRX since accumulation of TRX globules between dsDNA strands was occasionally observed, as shown in Supplementary Figure S3C. However, MDP1-TRX basically induced the same side-by-side DNA bundling as that observed during DNA compaction by $MDP1_{Msm}$ (Figure 3D). Compared with the HS-AFM images of the DNA/$MDP1_{Msm}$ complex, the DNA/MDP1-TRX complex exhibited additional globules (magenta) beside dsDNA (Figure 3D–F), which are thought to be the TRX globules. Therefore, we decided to use MDP1-TRX in order to follow the mIDR action during DNA compaction.

We carefully determined the number of HUR_{Msm} and TRX globules, acting together like a single molecule on dsDNA. Although previous X-ray crystallography of $MDP1_{Mtb}$ revealed an HU-like homodimer of HUR_{Mtb} (residues 1–99, PDB ID: 4PT4) (18), we frequently found sets of one HUR_{Msm} and one TRX (1HUR–1TRX), which are likely to be monomers (Figure 3G). We also reported that recombinant $MDP1_{Mtb}$ purified from *E. coli* was detected as a monomer in the phosphate-buffered solution, using the sedimentation velocity analytical ultracentrifugation (SV-AUC) and glutaraldehyde (GA)-cross-linking assay (19). We thus assessed the oligomeric states of MDP1 and related proteins used in this study, which were purified from *M. smegmatis* or *E. coli* by modified purification methods.

As we reported previously (19), SV-AUC in HS-AFM imaging buffer revealed that the vast majority (~98%) of $MDP1_{Mtb}$ was detected as monomers [1.46 S (28.9 kDa); Supplementary Figure S4A, $MDP1_{Mtb}$, m]. As for $MDP1_{Msm}$, the major peak occupying 71.1% of the total area under the curve (AUC) corresponded to a monomer [1.10 S (21.7 kDa); Supplementary Figure S4A, $MDP1_{Msm}$, m]. The peak corresponding to a dimer [d, 1.84 S (47.4 kDa)] was also detected (occupying 19.8%). Furthermore, TRX fusion did not alter the oligomeric state of MDP1 in solution (Supplementary Figure S4A, MDP1–TRX). Similarly, the majority of all these proteins were also detected as monomers in GA-cross-linking assay in PBS(–) (Supplementary Figure S4B).

We also examined the oligomeric state of $MDP1_{Msm}$ by electron microscopy (EM). Representative class-averaged images of negatively stained $MDP1_{Msm}$ are shown in Supplementary Figure S4C (EM). $MDP1_{Msm}$ HUR_{Msm} was mostly considered to have an identical structure to $MDP1_{Mtb}$ HUR_{Mtb} (PDB IDs: 4PT4 and 4KDY) since they exhibited high sequence similarity (98% positive, 93% identical, Figure 1A). In contrast, sequence similarity between mIDRs of these proteins is lower. Two different protein secondary structure predictions (Jpred4 and PSIPRED) showed both mIDRs as disordered regions (2). Accordingly, mIDR was invisible in the average images from the averaging process of single particle analysis. The 2D class averages of $MDP1_{Msm}$ exhibited L, v, y shaped structures, and they were consistent with projections simulated from the coordinates of a HUR_{Mtb} monomer (Supplementary Figure S4C, monomer), not a HUR_{Mtb} dimer (Supplementary Figure S4C, dimer). These observations further support the fact that, at least up to 12.5 μM, $MDP1_{Msm}$ is mostly a monomer in a physiological solution.

In contrast, *E. coli* HUα (an example of a HU dimer) purified using the same protocol was detected as a dimer by both SV-AUC [Supplementary Figure S4A, HUα, d, 1.61 S (20.6 kDa)] and GA-cross-linking assay (Supplementary Figure S4B, HUα), thus confirming that a monomeric form of MDP1 is not an artifact caused by the protein purification processes.

To deduce the mIDR action in the process of DNA compaction, we tracked the movement of the 1HUR–1TRX (monomeric MDP1-TRX) during DNA cross-linking events (Figure 3H; Supplementary Video S4). The 1HUR–1TRX sets moved along a dsDNA together, suggesting that DNA association of an $MDP1_{Msm}$ monomer was achieved by both HUR_{Msm} and stretched $mIDR_{Msm}$. When another dsDNA came close, TRX moved across another dsDNA or was located between two dsDNAs, and, finally, a single monomer (1HUR–1TRX set) cross-linked two dsDNAs together (Figure 3H). Thus, we could track the direction of $mIDR_{Msm}$ by the array of HUR_{Msm} and TRX globules. The location of the two globules (Figure 3I; Supplementary Figure S5A) gave us two possible DNA-bundling mechanisms: $mIDR_{Msm}$ either bands two dsDNAs together by lying across them or tapes two dsDNAs together by lying between them (Figure 3I). In addition, this DNA cross-linking is relatively stable, but also reversible (Supplementary Figure S5B).

CGMD model of the DNA cross-linking by MDP1 mIDR

Considering the highly positively charged mIDR, we subsequently investigated whether the DNA bundling could be explained by electrostatic attraction by means of CGMD simulations. Actually, multivalent cations are proposed to bind to multiple DNA duplexes (46). A miniature system to reproduce the HS-AFM observations was prepared; a 2100 bp supercoiled circular DNA was attached to a virtual HS-AFM substrate by Lennard–Jones potential, and 10 $MDP1_{Msm}$ molecules were placed around the DNA. Electrostatic interactions and excluded volume effects were then defined between DNA and $MDP1_{Msm}$ (for details, see the Materials and methods; Supplementary Figure S6; Supplementary Table S4).

In the simulations, early-stage DNA compaction was observed (Figure 4A; Supplementary Videos S5–S7; final snapshots of all 10 trajectories are also shown in Supplementary Figure S7). Three major types of structures were observed,

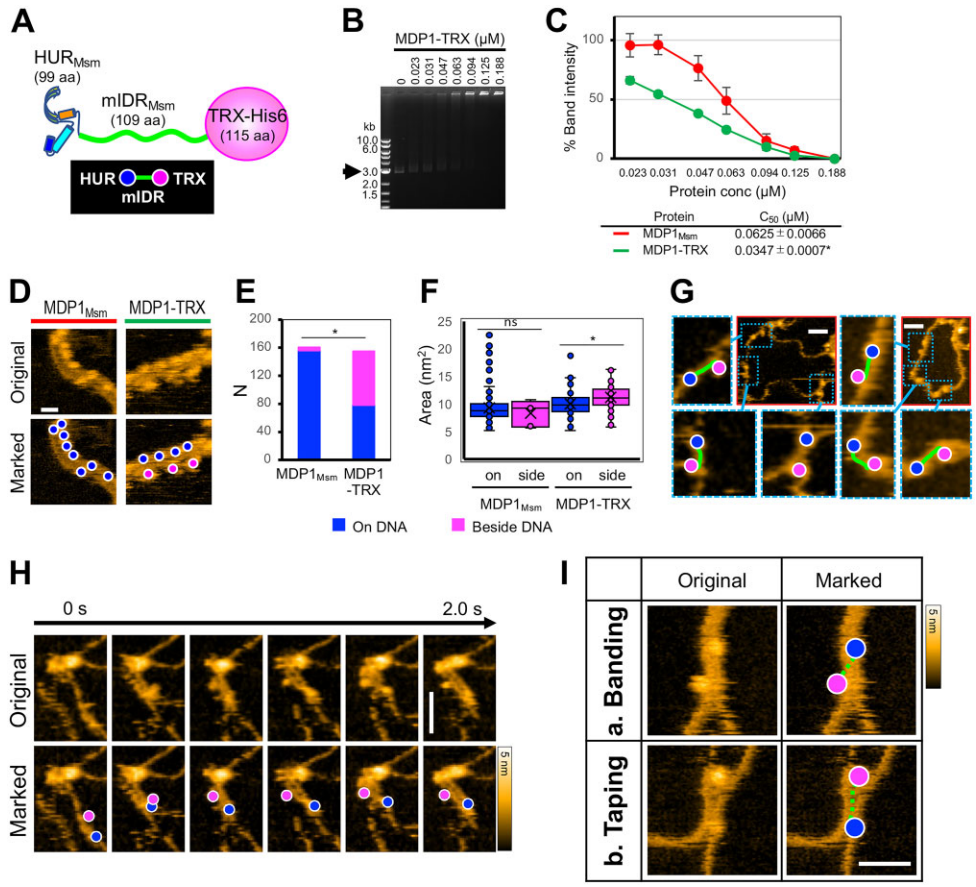

Figure 3. Following the mIDR action during DNA cross-linking by HS-AFM time-lapse imaging using a globular tag. (**A**) Cartoon image of MDP1-TRX [referring to HUR_{Mtb} (PDB ID: 4DKY)]. In the following HS-AFM images, HUR_{Msm} and TRX globules are marked with blue and magenta, respectively. The deduced position of $mIDR_{Msm}$ is marked with green. (B and C) Affinity of $MDP1_{Msm}$ and MDP1-TRX for the supercoiled plasmid (gel retardation assay). A representative of triplicate gels is shown (**B**). Band intensity (mean ± SD, $n = 3$) and C_{50} (mean ± SD, $n = 3$) were calculated (**C**), as described in Figure 1B. $^*P < 0.05$, compared with $MDP1_{Msm}$ (ANOVA). (D–F) Comparison of DNA/$MDP1_{Msm}$ and DNA/MDP1-TRX complexes by HS-AFM. Representative HS-AFM images are shown (**D**, 5 fps). Bar, 10 nm. In the lower panels, HUR_{Msm} and TRX are marked. Using the HS-AFM images (5 fps) of DNA/$MDP1_{Msm}$ and DNA/MDP1-TRX complexes, the number (N) of globules localized on and beside DNA were counted (**E**). N = 161 for $MDP1_{Msm}$ and 155 for MDP1-TRX ($^*P < 0.05$, χ^2 test). The size distribution of the globules found on and beside dsDNA were also measured using Image J Fiji (**F**), as described in the Materials and methods ($^*P < 0.05$; ns, not significant; Mann–Whitney test). (**G**) Examples of 1HUR-1TRX sets. Red boxes, original HS-AFM time-lapse images of DNA/MDP1-TRX complexes (5 fps, formed in the presence of 1.4–12.5 nM MDP1-TRX); blue-dashed boxes, examples of 1HUR (blue)–1TRX (magenta) sets magnified from the red boxes. Bars, 30 nm. (**H**) The movement of the single 1HUR–1TRX set during DNA cross-linking, captured by HS-AFM at 5 fps. Upper, original images; lower, marked images. The corresponding movie is presented in Supplementary Video S4. Bar, 30 nm. (I) $mIDR_{Msm}$ positions deduced from the arrays of HUR_{Msm} and TRX on cross-linked dsDNAs. Left, original images; right, marked images. Deduced $mIDR_{Msm}$ positions are indicated as dashed green lines. Bar, 20 nm. Other examples are also shown in Supplementary Figure S5A. See also Supplementary Figures S3–S5; Supplementary Video S4; and Supplementary Table S3.

all of which were seen in HS-AFM observations. In the first structure, $MDP1_{Msm}$ was simply bound to DNA, where its $mIDR_{Msm}$ extends along dsDNA (for instance, Figure 4A left top area of $MDP1_{Msm}$). In the second structure, $MDP1_{Msm}$ molecules were clustered at DNA intersects (shown by arrows in Figure 4A). Similar clusters of MDP1 molecules at DNA intersects were also seen in HS-AFM analysis (Figure 1C). However, mIDR action at DNA intersects was not clarified by HS-AFM analysis. Lastly, dsDNAs were cross-linked by $MDP1_{Msm}$ in the third structure (Figure 4A, $MDP1_{Msm}$, and B). In DNA cross-linking by an $MDP1_{Msm}$ monomer (Figure 4B; Supplementary Video S8a), first $MDP1_{Msm}$ tightly bound to a dsDNAs (Figure 4B, top). $mIDR_{Msm}$ also bound to another dsDNA that came close to it (Figure 4B, middle). Finally, almost the full length of mIDR bound both dsDNAs like a 'double-sided tape' (Figure 4B, bottom). This final structure concurs with the HS-AFM data of Figure 3I-b. In some of the cross-linking regions, multiple $MDP1_{Msm}$ molecules were lined up in series and lengthened the DNA bundle, which successfully reproduced the DNA compaction observed in our HS-AFM imaging (Figure 4C). DNA cross-linking by $mIDR_{Msm}$ further brings upstream and downstream regions of two dsDNAs in proximity. This could promote the next cross-linking by another $MDP1_{Msm}$ molecule (Supplementary Video S8b). Such a cascade of cross-linking is a possible mechanism for a long-range, side-by-side bundling of dsDNAs (like zipping; Figure 1C). Therefore, CGMD simulations proposed the mechanism of DNA compaction by MDP1, where MDP1 mIDR got between two DNA duplexes and cross-linked the DNAs in a 'double-sided tape' manner. In addition, electrostatic interactions were sufficient to drive the compaction.

The same simulations were also performed with MDP1-TRX (Figure 4A, MDP1-TRX; Supplementary Video S6). Af-

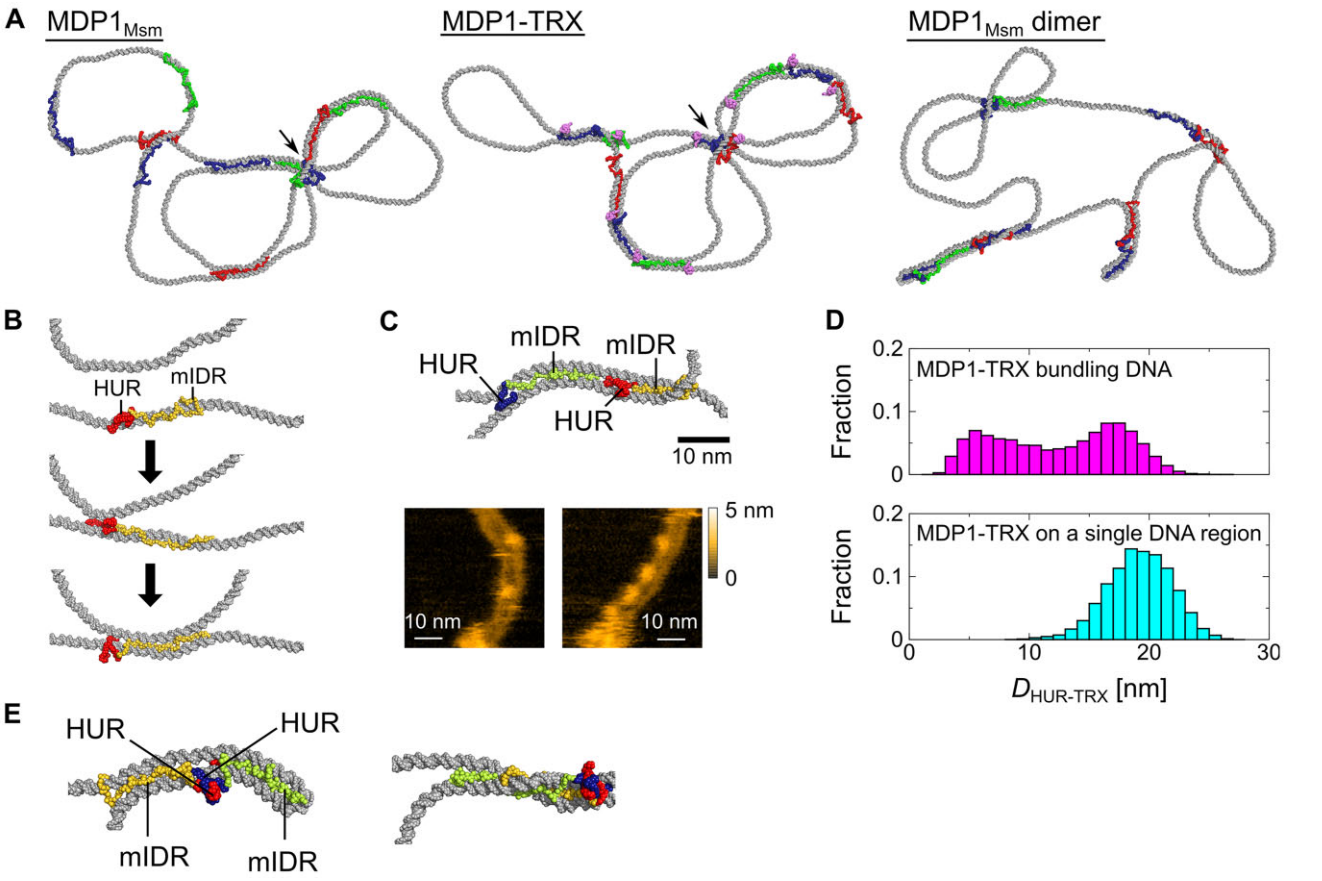

Figure 4. Double-sided tape-like DNA cross-linking model by MDP1 mIDR. (**A**) CGMD snapshots of the virtual HS-AFM system. Representative snapshot of plasmid and $MDP1_{Msm}$ monomers (left), plasmid and MDP1-TRX monomers (middle) and plasmid and $MDP1_{Msm}$ dimers (right). A simulation movie is also presented in Supplementary Videos S5–S7. These views are from above; the structures are viewed from the direction perpendicular to the virtual AFM substrate. DNAs are drawn in silver. For visibility, each $MDP1_{Msm}$ molecule was drawn in red, dark blue or green. TRX-tags are drawn in pink. Arrows indicate DNA intersections where $MDP1_{Msm}$ and MDP1-TRX molecules are bound. (**B**) Magnified view of DNA compaction by a single $MDP1_{Msm}$ monomer. A simulation movie is presented in Supplementary Video S8a. Here, HUR_{Msm} and $mIDR_{Msm}$ of $MDP1_{Msm}$ are drawn in red and yellow, respectively. (**C**) Upper: a structural model of DNA compaction by multiple $MDP1_{Msm}$ monomers observed in the CGMD simulations. A simulation movie is presented in Supplementary Video S8b. One MDP1 monomer is drawn in red (HUR_{Msm}) and yellow ($mIDR_{Msm}$), and the other is drawn in dark blue (HUR_{Msm}) and yellowish green ($mIDR_{Msm}$). Lower: examples of HS-AFM images. Bars, 10 nm. (**D**) Distance distributions between the HUR_{Msm} and TRX-tag ($D_{HUR\text{-}TRX}$). Upper: the distribution for MDP1-TRX which bundles multiple DNA regions. Lower: the distribution for MDP1-TRX bound to a DNA region without bundling the DNA. (**E**) Representative structures of dimeric $MDP1_{Msm}$ cross-linking DNA duplexes. The two mIDRs are bound to the DNA in the opposite direction (left), or they are bound to the DNA in the same direction (right). The color code is the same as in (C). See also Supplementary Figures S6 and S7; and Supplementary Videos S5–S8.

ter checking the reproducibility of the 'double-sided tape' cross-linking which was also observed by HS-AFM, the conformation of the $mIDR_{Msm}$ was evaluated with the distance between the HUR_{Msm} and TRX-tag. In cases where $MDP1_{Msm}$ bundled multiple DNA regions, two peaks appeared in the distribution of the distance between HUR_{Msm} and TRX ($D_{HUR\text{-}TRX}$, Figure 4D, top). The peak around 5 nm can be interpreted as the distance of the compact $MDP1_{Msm}$ structure at the DNA intersects, and the one around 17 nm corresponds to extended $MDP1_{Msm}$ of the 'double-sided tape' cross-linking. Compared with the cross-linking cases, $D_{HUR\text{-}TRX}$ was likely to be larger when $MDP1_{Msm}$ was bound to DNA without cross-linking (Figure 4D, bottom).

Although ~20% of MDP1 proteins form dimers in solution (Supplementary Figure S4A, $MDP1_{Msm}$, d), it was difficult to detect the dimer with HS-AFM. Therefore, DNA compaction by $MDP1_{Msm}$ dimers was examined by CGMD simulation. As seen in the plasmid/$MDP1_{Msm}$ monomer simulation, the 'double-sided tape' cross-linking events were also observed (Figure 4A, $MDP1_{Msm}$ dimer; Supplementary Video S7). In this model, two types of $mIDR_{Msm}$ locations were observed: one extending in the opposite direction to each other and the other extending in the same direction (Figure 4E).

Taken together, 'double-sided tape' DNA cross-linking by mIDR is the mechanism responsible for DNA compaction by both monomeric and dimeric MDP1. Thus, our findings reveal a totally different way of DNA compaction from those of previously reported HUs and other DNA-binding proteins.

mIDR length-dependent DNA compaction and growth suppression

We further investigated the structure–activity relationship of mIDR. mIDR is composed of 17–19 amino acid repeat-like sequences (including one or two PAKK repeats, Supplementary Figure S1A). We constructed $MDP1_{Msm}$ mutants whose $mIDR_{Msm}$ was truncated at every repeat from the C-terminus (Figure 5A, $T191_{Msm}$–$T109_{Msm}$). These mutants and full-length $MDP1_{Msm}$ were inducibly expressed and purified from

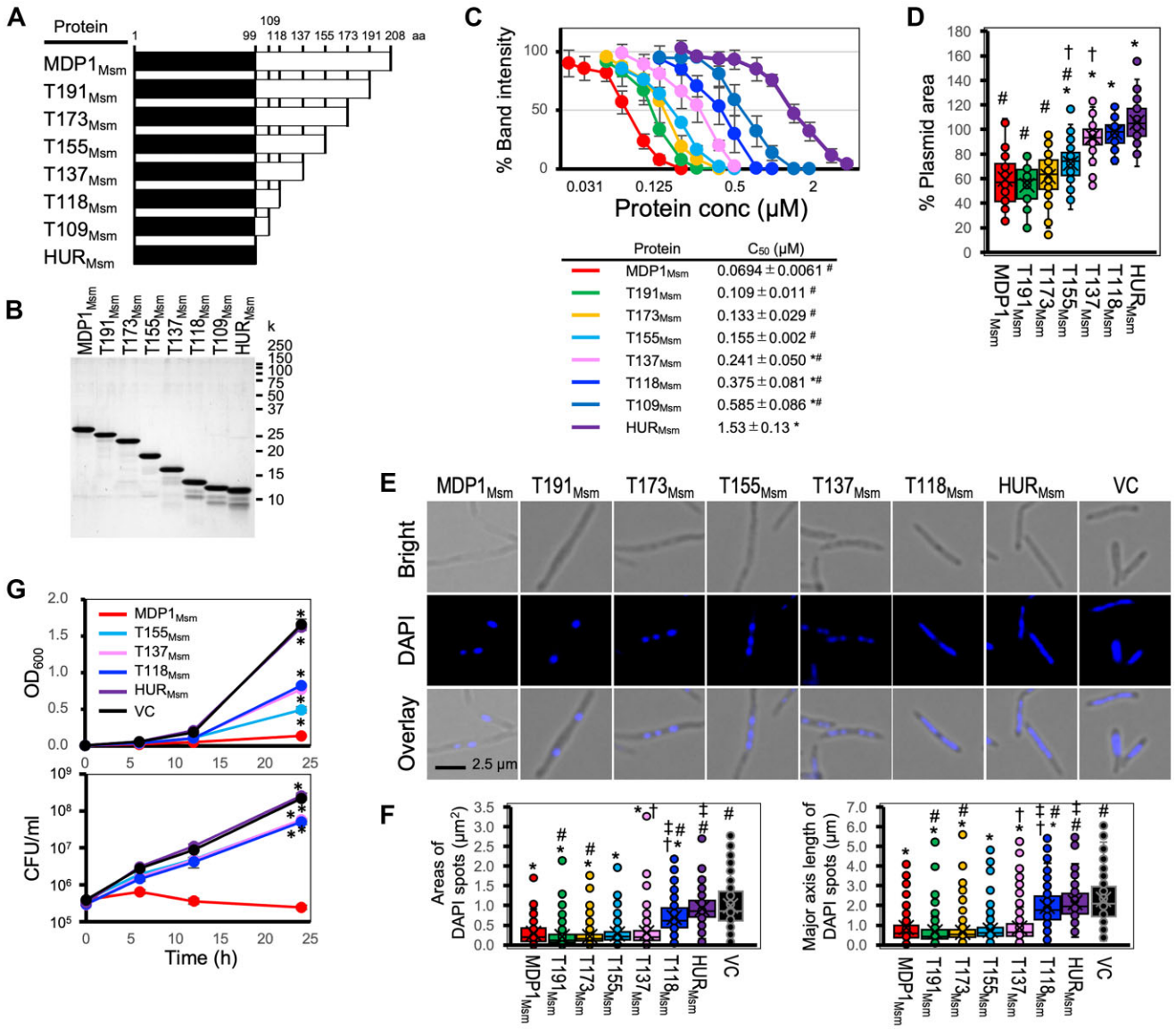

Figure 5. mIDR length-dependent DNA binding and compaction by MDP1. (A and B) Schematic representation (**A**) and SDS–PAGE (**B**) of $mIDR_{Msm}$-truncated mutants of $MDP1_{Msm}$. (**C**) Affinity of $mIDR_{Msm}$-truncated mutants for supercoiled plasmid (gel retardation assay). Representative gels are shown in Supplementary Figure S8A. Band intensity (mean ± SD, $n = 3$) and C_{50} (mean ± SD, $n = 3$) were calculated as described in Figure 1B. * and #, $P < 0.05$ compared with $MDP1_{Msm}$ and HUR_{Msm}, respectively (ANOVA). (**D**) Plasmid compaction by each mutant, as described in Figure 1D ($n \geq 22$). *$P < 0.05$ compared with $MDP1_{Msm}$ and #$P < 0.05$ compared with HUR_{Msm}. †$P < 0.05$ (Kruskal–Wallis test and Mann–Whitney test). (E and F) Chromosome compaction after 24 h induction of $mIDR_{Msm}$-truncated $MDP1_{Msm}$ mutants in the *Msm* Δ*mdp1* strain. Representative fluorescence microscopic images are presented (**E**). The area and major axis length of individual 4′,6-diamidino-2-phenylindole (DAPI)-stained spots were measured and plotted ($n \geq 220$ each, **F**). VC, vector control. *$P < 0.05$ compared with VC. #$P < 0.05$ compared with $MDP1_{Msm}$. † and ‡, $P < 0.05$ (Kruskal–Wallis test and Wilcoxon test). (**G**) Bacterial growth (OD_{600} and CFU) after induction of each protein. Mean ± SD, $n = 3$. *$P < 0.05$ compared with $MDP1_{Msm}$ (ANOVA). See also Supplementary Figure S8 and Supplementary Table S3.

Msm Δ*mdp1* (Figure 5B). We observed that only the first 10 residues of mIDR ($T109_{Msm}$) were sufficient to increase DNA affinity, but the affinity was basically dependent on mIDR length, and full-length $MDP1_{Msm}$ showed the highest affinity for DNA compared with any other mutants (Figure 5C; Supplementary Figure S8A–C; and Supplementary Table S3).

We next investigated DNA compaction by these mutants using HS-AFM. When treating plasmids with shorter $mIDR_{Msm}$ mutants, the plasmids showed less bundled regions (Supplementary Figure S8D). Compaction of the plasmids was basically mIDR length dependent (Figure 5D). However, $T173_{Msm}$ and $T191_{Msm}$ mutants showed similar DNA compaction activity as full-length $MDP1_{Msm}$. $T137_{Msm}$ and $T118_{Msm}$ mutants almost lost DNA compaction activity and their activities are comparable with that of HUR_{Msm}. The $T155_{Msm}$ mutant showed intermediate activity. In addition, a large difference was observed between $T155_{Msm}$ (56 residues in mIDR) and $T137_{Msm}$ (38 residues in mIDR).

We further investigated bacterial phenotypes after induction of the full-length $MDP1_{Msm}$ and mutant proteins in *Msm* Δ*mdp1* (Supplementary Table S2) (2). As for chromosome compaction, similar compacted DAPI-stained DNA

spots were observed in bacteria expressing either intact MDP1 or $T137_{Msm}$–$T191_{Msm}$ mutants (≥38 residues of $mIDR_{Msm}$; Figure 5E, F). mIDR length dependency was also seen in growth-suppressive activity (Figure 5G).

Taken together these results suggest that the DNA affinity of MDP1 is totally dependent on mIDR length, but a certain length of mIDR is sufficient for DNA compaction *in vitro* and in bacteria.

The amino acid composition of mIDRs is similar among mycobacterial species, although the sequence similarity is relatively low (Figure 1A; Supplementary Figure S1B). The $mIDR_{Mtb}$-truncated mutants of $MDP1_{Mtb}$ (Supplementary Figure S8E, F, $T188_{Mtb}$–$T118_{Mtb}$) showed similar $mIDR_{Mtb}$ length dependency in DNA affinity (Supplementary Figure S8G, H), whereas a shorter length $mIDR_{Mtb}$ (≥44 residues; $T143_{Mtb}$–$T188_{Mtb}$) was enough to induce chromosome compaction in bacteria (Supplementary Fig. S8I, J), suggesting that similar properties are conserved in MDP1s.

mIDR hijacks the HU functions

HUs are conserved in eubacteria but do not possess an MDP1-like IDR (14). Our data suggest the possibility that MDP1 mIDR dominates HU function. To test this hypothesis, we constructed fusion proteins of *E. coli* HUs with $mIDR_{Msm}$ (Figure 6A, HUα-mIDR and HUβ-mIDR) and checked their property. GA-cross-linking assay showed that $mIDR_{Msm}$ fusion did not alter the dimerization of *E. coli* HU (Supplementary Figure S4B, HUα-mIDR). As expected, gel retardation assay demonstrated that fusion of *E. coli* HUs with $mIDR_{Msm}$ increased DNA affinity, which is comparable with that of $MDP1_{Msm}$ (Figure 6B, C; Supplementary Table S3). Monitoring DNA compaction by HS-AFM showed that a significant change in plasmid conformation was not induced by HUα (Figure 6D, E; Supplementary Video S9). In clear contrast, DNA was compacted by the fusion protein of HUα and $mIDR_{Msm}$ (Figure 6D, E; Supplementary Video S9), indicating that $mIDR_{Msm}$ can hijack HU function and make $mIDR_{Msm}$ function dominant in the fusion protein.

mIDR induces mycobacterial dormancy

Our data show that mIDR is critical for MDP1-mediated DNA compaction by the 'double-sided tape' model and growth arrest. Finally, we tested if MDP1 and mIDR induce bacterial dormancy. Using inducible protein expression in *Msm* Δ*mdp1*, we evaluated the effect of intact $MDP1_{Msm}$ and $mIDR_{Msm}$ fusion of HU on bacterial growth and viability by measuring the optical density at 600 nm (OD_{600}), colony-forming units (CFU), and by SYTO9 and propidium iodide (PI) staining, followed by flow cytometry analysis.

$MDP1_{Msm}$ expression suppressed the bacterial OD_{600} (Figure 6F). This growth suppression was not due to bacterial death because the reduction of the bacterial CFU (Figure 6F) and increase of PI-positive cells (Figure 6G, H) were low. Despite heterogenous expression, either HUα or HUβ induced moderate reduction of bacterial growth (Figure 6F). In contrast, the $mIDR_{Msm}$ fusion proteins (HUα-mIDR and HUβ-mIDR) induced much stronger CFU reduction than $MDP1_{Msm}$ (Figure 6F) without a considerable increase of PI-positive cells in flow cytometry (Figure 6G, H). This indicates that mIDR can induce the non-replicating dormant state.

Discussion

In this study, we observed the DNA compaction processes by MDP1 via real-time imaging by HS-AFM. We found that MDP1 cross-linked two adjacent dsDNAs by mIDR and bundled a long-range of dsDNAs side-by-side like zipping (Figures 1–3). MDP1 further formed raft-like multiple DNA bundles, and consequently compacted an entire plasmid. We revealed a 'double-sided tape' DNA cross-linking model by MDP1 mIDR via a combination of HS-AFM imaging of MDP1–TRX and modeling by CGMD simulation (Figures 3 and 4). Our results indicate that mIDR-mediated 'double-sided tape' DNA cross-linking dominates MDP1 functions and can induce resuscitable non-replicating dormant bacteria.

In this study, HS-AFM imaging revealed that MDP1 compacted DNA by cross-linking adjacent dsDNAs side-by-side like zipping (Figure 1C). This MDP1 activity preferentially compacted supercoiled DNA (Figure 1F, G). It has been reported that negative supercoiling tension itself naturally causes the compaction of cosmid-size circular DNAs (>10 kb) into hyperplectonemes of multiple DNA strands (41). However, such negative supercoiling tension of DNA is not likely to be required for MDP1 to induce DNA cross-linking since $MDP1_{Msm}$ bundled dsDNA strands located in close proximity, including the relaxed or linear DNAs which have no negative supercoiling tension (Figure 1F, G). Our structural model of DNA cross-linking by MDP1 also supports this result. Our model indicates that electrostatic interaction is enough to induce DNA compaction (Figure 4). It also shows that the $MDP1_{Msm}$ monomer did not compact the open DNA region by DNA bending (Figure 4). These findings indicate that MDP1 simply cross-links dsDNA strands located in close proximity via electrostatic interaction, and negative supercoiling tension facilitates DNA compaction by MDP1 through locating DNA strands in close proximity.

We previously reported that induction of $MDP1_{Msm}$ expression stimulates dormant phenotypes in mycobacteria, including mIDR-dependent chromosome compaction (2). In addition to the results within bacteria, our study revealed mIDR-dependent DNA compaction *in vitro* (Figure 2D, E). mIDR alone not only bound to DNA (Figure 2C; Supplementary Figure S2), but also compacted the plasmid (Figure 2D, E), unlike HUR which does not have such activity. Actually, relatively wide DNA regions between HUR globule-binding sites were intertwined (Figure 2H). Thus, mIDR is responsible for MDP1-mediated DNA compaction.

We further investigated the mIDR action experimentally by employing TRX-tag at the C-terminus of $MDP1_{Msm}$ $mIDR_{Msm}$ using HS-AFM time-lapse imaging (Figure 3). TRX-His6-tag is a 12.6 kDa protein and therefore, due to steric hindrance, it partially interfered with the whole plasmid compaction compared with $MDP1_{Msm}$ (Supplementary Figure S3). However, the size of TRX was required to distinguish it from other structures under HS-AFM. TRX was also distinguishable from HUR because the TRX–DNA association pattern was clearly different from that of HUR. Importantly, TRX fusion did not affect DNA affinity and cross-linking of $MDP1_{Msm}$ (Figure 3B–D; Supplementary Table S3). This approach thus allowed us to carry out single molecular analysis of mIDR action during DNA cross-linking by following the array of HUR and TRX globules (Figure 3H). This single molecular analysis

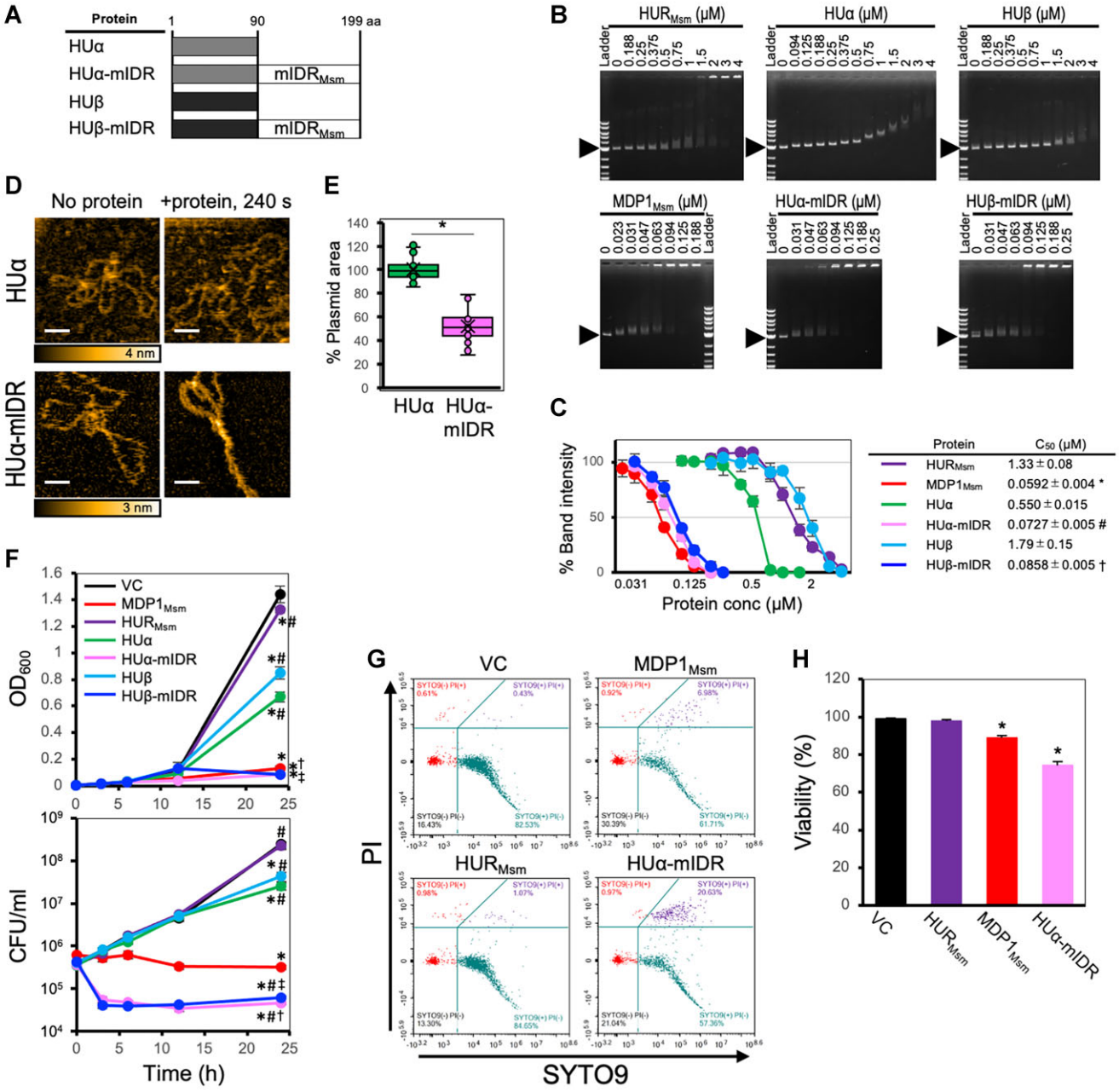

Figure 6. mIDR-mediated DNA cross-linking induces bacterial dormancy phenotype by hijacking the HU functions. (**A**) Schematic representation of *E. coli* HUs and their fusion proteins with $mIDR_{Msm}$. (**B** and **C**) Affinity of *E. coli* HUs and their fusion proteins for supercoiled plasmid (gel retardation assay). Representatives of triplicate gels are shown (B). Band intensity (mean ± SD, $n = 3$) and C_{50} (mean ± SD, $n = 3$) were calculated (C), as described in Figure 1B. $^{*}P < 0.05$, compared with HUR_{Msm}. $^{\#}P < 0.05$, compared with HUα. $^{\dagger}P < 0.05$, compared with HUβ (ANOVA). (**D**) HS-AFM time-lapse imaging of plasmid morphological changes induced by HUα and HUα-mIDR (5 fps). Left, protein-free; right, incubated with the proteins. Bars, 60 nm. Time-lapse movies are presented in Supplementary Video S9. (**E**) Plasmid compaction as described in Figure 1D ($n = 23$). $^{*}P < 0.05$ (Mann–Whitney test). (**F**) Bacterial growth (OD_{600} and CFU) after induction of the indicated protein. $^{*}P < 0.05$, compared with VC; $^{\#}P < 0.05$, compared with $MDP1_{Msm}$; $^{\dagger}P < 0.05$, compared with HUα; $^{\ddagger}P < 0.05$, compared with HUβ (mean ± SD, $n = 3$, ANOVA). (**G** and **H**). Flow cytometric analysis of the viability of mycobacterial cells expressing $MDP1_{Msm}$, HUR_{Msm} and HUα-mIDR. After 24 h induction of the indicated protein, mycobacterial cells were stained with SYTO9 and PI. Representative flow cytometry plots of triplicate cultures are shown (G). Bacterial viability was calculated from flow cytometric data (H). Both $PI^{+}/SYTO9^{-}$ and $PI^{+}/SYTO9^{+}$ mycobacterial cells were considered as dead cells, whereas $PI^{-}/SYTO9^{+}$ were considered as live cells. Unidentified cells ($PI^{-}/SYTO9^{-}$) were excluded from the calculation. Mean ± SD ($n = 3$). $^{*}P < 0.05$, compared with VC (ANOVA). See also Supplementary Video S9 and Supplementary Table S3.

successfully revealed two possible DNA cross-linking mechanisms (banding or taping two dsDNAs together by mIDR) (Figure 3I).

In this study, we also conducted CGMD simulation of a mini-plasmid/$MDP1_{Msm}$ system (Figure 4A). CGMD simulation successfully reproduced the plasmid/$MDP1_{Msm}$ complex structures observed by HS-AFM imaging and clarified the detailed molecular mechanisms of the DNA cross-linking by $MDP1_{Msm}$ $mIDR_{Msm}$ (Figure 4B). Our simulation revealed that $mIDR_{Msm}$ cross-links dsDNAs together by electrostatic interaction in a 'double-sided tape' manner, which is one of the mechanisms proposed using MDP1-TRX (Figure 3I). This is a reasonable model for MDP1 to cross-link DNA even in a monomeric form and to even hijack the function of HU (Figures 4B and 6). Our model also explains well the mIDR length dependency and low DNA sequence specificity of DNA binding and cross-linking by MDP1. In addition, the CGMD simulation demonstrated more compacted conformations of $mIDR_{Msm}$ at DNA intersects, which could not be observed by HS-AFM (Figure 4A, arrow). At the DNA intersects, multiple DNA strands are crossing in various directions. A single $mIDR_{Msm}$ could naturally fit into a compacted conformation by associating with multiple DNA strands partially in a double-sided tape manner or via simple electrostatic interaction. Based on the similar amino acid compositions (Supplementary Figure S1B), MDP1 mIDR was thought to have similar functional properties to that of histone H1 C-IDR_{H1} (14,27,47). However, C-IDR_{H1} conformation is more compacted by fitting in a steric space of the nucleosome *in vivo* (48). This is in sharp contrast to the environment of DNA/MDP1 mIDR complex formation. Electrostatic interaction-mediated 'double-sided tape' DNA cross-linking is a newly observed mode of action in the compaction of bacterial chromosome without chromatin structure.

Similar filamentous DNA bundling has been observed in the conventional AFM analysis of a DNA complex with H-NS, which is generally known as a homodimer protein (40,43). Arold *et al*. reported that, in a DNA/H-NS complex, H-NS homodimers are further assembled into a rigid superhelical scaffold which is parallelly sandwiched by two dsDNAs via a DNA-binding helix–turn–helix structure of each protomer (49). Such a rigid and long-range DNA/H-NS/DNA superhelix represses expression of genes involved in the superhelix (40). Therefore, H-NS overexpression causes a lethal phenotype of *E. coli* (50). Meanwhile, in this study, our data propose that the accumulation of 'double-sided tape' DNA cross-linking by MDP1 mIDR induces a long-range zipper-like DNA bundling. These bundled DNAs are further bundled into a raft-like bundle of multiple dsDNAs (Figure 1C), which is theoretically impossible to be formed by a DNA/H-NS/DNA superhelix. However, MDP1 on the compacted DNA strands did not look like a rigid scaffold-like structure; rather individual monomers moved more flexibly on the DNA strands (Supplementary Video S3). Moreover, DNA cross-linking by MDP1 is likely to be reversible (Supplementary Figure S5B). In agreement with the DNA compaction model and our observations, we found that MDP1 down-regulates a wide variety of genes that are widely distributed in the mycobacterial genome (51,52). However, MDP1 overexpression is not lethal for mycobacteria, rather it induces the viable but not culturable cell (VNC)-like non-replicating bacteria (Figure 6F–H). The reversible and flexible structure of the DNA/MDP1 complex is likely to facilitate the transcription machinery to access the minimal essential genes to maintain the bacterial persistence. 'Double-sided tape' DNA cross-linking and zipper-like long-range DNA bundling mediated by MDP1 mIDR could be a novel and reasonable DNA compaction mechanism that leads to formation of resuscitable non-replicating dormant bacteria.

It has also been reported that bacterial RNA-binding protein Hfq binds to DNA and induces filamentous DNA compaction via an unstructured C-terminal tail (53,54). Unlike MDP1 mIDR, Hfq C-terminal tail has the characteristic of amyloids (55). It has been reported that Hfq forms an amyloid-like complex with DNA (56). Therefore, the mechanism of DNA/Hfq complex formation may differ from that of DNA/MDP1 complex although the details remain unclear. Further investigations of the structures and mechanisms of the DNA complexes of such DNA-binding proteins including MDP1 will further deepen our understanding of the regulation of chromosome structure in various species.

This study and our previous study (19) consistently revealed that the majority of MDP1 is a monomer in the tested conditions (protein purification methods, buffer systems and protein concentration ranges). It remains unclear why the majority of MDP1 molecules exist as monomers in solution. Comparison of X-ray crystallographic data of HU dimer (17) and $MDP1_{Mtb}$ HUR_{Mtb} dimer (18) does not indicate any clear difference in the interaction between two protomers. In our previous report (19), SV-AUC revealed that $MDP1_{Mtb}$ is a monomer in phosphate buffer containing 150–500 mM salt concentrations. MDP1 is also a monomer in HS-AFM imaging buffer whose salt concentration is 80 mM (Supplementary Figure S4A). In contrast, since ∼30% of HUR_{Mtb} formed dimers at 500 mM salt (19), mIDR probably has the potential to inhibit HUR dimerization. However, this cannot also explain the difference from HU since HUR is mostly a monomer in PBS(–) too (Supplementary Figure S4B) (19). Further structural study is required to answer this question.

In addition, the function of monomeric HUR remains unknown. Even in the monomeric form, HUR slightly contributed to DNA affinity, but not DNA compaction (Figure 2C–E; Supplementary Figure S2). However, HUR-deficient $mIDR_{Msm}$ exhibited more efficient and unusual bundling of multiple dsDNAs, compared with intact $MDP1_{Msm}$, and unstructured accumulation on bundled dsDNAs (Figure 2D–F). We cannot eliminate the possibility that $mIDR_{Msm}$ might spread more easily on mica in the absence of HUR_{Msm} and therefore might be able to take action more efficiently than intact $MDP1_{Msm}$. However, it is also possible to think that HUR contributes to the restriction of mIDR actions along dsDNA. Although the details are still unknown, this might be a possible role for the monomeric HUR. On the other hand, we do not disregard the role of HUR dimerization in MDP1 functions. Our data indicate that the equilibrium between monomer and dimer favors a monomer under conditions tested in this study (Figure 3; Supplementary Figure S4). On the other hand, X-ray crystallographic data of $MDP1_{Mtb}$ HUR_{Mtb} dimer (18) suggests that more crowded conditions induce HUR dimerization. Our MD simulation revealed that even in a dimeric form, MDP1 cross-links two dsDNAs via a 'double-sided tape' model (Figure 4E). However, constitutively dimerized *E. coli* HU–mIDR fusion proteins exhibited enhanced VNC induction (Figure 6F–H), suggesting that HUR dimerization could contribute to growth suppression synergistically with mIDR in the mycobacterial cells. Expression of HUα–mIDR caused significantly more mycobacterial death

than that by $MDP1_{Msm}$ (Figure 6G, H), although mycobacterial death was not a major cause of large CFU reduction by fusion protein expression (Figure 6F). MDP1 HUR may have evolved into a structure more suitable to regulate mycobacterial dormancy and resuscitation with minimal loss of viability.

Here, we revealed a novel and dynamic double-sided tape DNA cross-linking by MDP1 mIDR, followed by zipper-like long-range DNA bundling, which may play a role in the formation of resuscitable VNC-like dormant mycobacteria. MDP1 is essential for *Mtb* growth (57) and contributes to, for example, long-term survival and isoniazid tolerance in mycobacteria (2,11,51), suggesting an attractive drug target for mycobacterial diseases. Our model provides an important insight into drug development against intractable mycobacterial diseases including drug-tolerant latent states. In addition, according to the sequence database (NCBI, https://www.ncbi.nlm.nih.gov), HU orthologs of some other environmentally slow-growing or stress-resistant bacteria (such as *Nocardia* spp., *Streptomyces* spp. and *Deinococcus* spp.) also possess a similar polycationic tail at the C- or N-terminus of their HU-like region. Therefore, the modulation of genomic structure and functions via our DNA cross-linking model by these polycationic IDRs of HU could be a common mechanism for such bacteria to persist under environmental stresses.

Data availability

The data underlying this article are available from the corresponding authors on reasonable request.

Supplementary data

Supplementary Data are available at NAR Online.

Acknowledgements

We thank Professor Toshio Ando for the use of the facilities at WPI NanoLSI, Kanazawa University and his technical support with HS-AFM experiments. All molecular dynamics simulations were performed with a computer cluster in Kyoto University. We thank Professor Shoji Takada for providing the computational resource; Professor Fumio Arisaka (Nihon University) for SV-AUC analysis and useful discussions about the manuscript; D. Tsuyoshi Shirai (Nagahama Institute of BioScience and Technology) for useful discussions and manuscript correction of EM data; Dr Shuhei Tomita (Osaka Metropolitan University Graduate School of Medicine) for use of the facility; Ms Haruka Kobayashi, Ms Yuko Ito, Mr Tomohiro Kon, Ms Yoko Kobayashi, Mr Takeshi Morishita, Mr Hiroaki Muto, Mr Junya Watanabe, Mr Kodai Yamazaki, Mr Yusuke Ota, Mr Mamoru Nishida, Dr Ann Savitskaya, Dr Aleksandr Ilinov, Ms Mika Shioya, and Ms Yoshimi Meguro (Niigata University) for their technical assistance; and Ms Yuko Kobayashi (Niigata University) for her kind support. We also thank Professor Kosuke Morikawa (Kyoto University) for useful discussion about this study and proofreading the manuscript.

Author contributions: A.N. and S.M. conceived the project and coordinated partner contributions. A.N., N.K., T.N. and M.S. performed HS-AFM analysis. M.S. performed GCMD simulation. K.M. performed electron microscopy. A.N., Y.O., A.Y., T.Y., M.H., S.A.K, K.I., Y.T. and S.M. performed all other molecular biology and biochemistry work. A.N., S.M., N.K., M.S., T.Y., S.A.K., K.I. and K.M. wrote the manuscript with input from all authors.

Funding

The Japanese Ministry of Education, Culture, Sports, Science and Technology [MEXT, 17K08823 to A.N., 20H03483 to S.M. and 20K22629 to M.S.]; the Japan Agency for Medical Research and Development [AMED, Research Program on Emerging and Re-emerging Infectious Diseases, JP20fk0108090 to A.N., JP20fk0108089 to S.M.; and AMED-CREST, JP22gm1610009 to S.M.]; the Japan Science and Technology Agency [JST, JPMJCR1762 to N.K.); Niigata University Interdisciplinary Research (U-go) [grants to A.N., K.I. and N.K.]; the World Premier International Research Center Initiative (WPI, MEXT, Japan, Kanazawa University); and the Cooperative Research Project Program of the Medical Institute of Bioregulation, Kyushu University [K.M. and S.M.].

Conflict of interest statement

All authors declare no competing interest.

References

1. Pirofski,L. and Casadevall,A. (2020) The state of latency in microbial pathogenesis. *J. Clin. Invest.*, **130**, 4525–4531.
2. Savitskaya,A., Nishiyama,A., Yamaguchi,T., Tateishi,Y., Ozeki,Y., Nameta,M., Kon,T., Kaboso,S.A., Ohara,N., Peryanova,O.V., *et al.* (2018) C-terminal intrinsically disordered region-dependent organization of the mycobacterial genome by a histone-like protein. *Sci. Rep.*, **8**, 8197.
3. Wolf,S.G., Frenkiel,D., Arad,T., Finkel,S.E., Kolter,R. and Minsky,A. (1999) DNA protection by stress-induced biocrystallization. *Nature*, **400**, 83–85.
4. Loiko,N., Danilova,Y., Moiseenko,A., Kovalenko,V., Tereshkina,K., Tutukina,M., El-Registan,G., Sokolova,O. and Krupyanskii,Y. (2020) Morphological peculiarities of the DNA–protein complexes in starved *Escherichia coli* cells. *PLoS One*, **15**, e0231562,
5. Frenkiel-Krispin,D., Ben-Avraham,I., Englander,J., Shimoni,E., Wolf,S.G. and Minsky,A. (2004) Nucleoid restructuring in stationary-state bacteria. *Mol. Microbiol.*, **51**, 395–405.
6. Rafiei,N., Cordova,M., Navarre,W.W. and Milstein,J.N. (2019) Growth phase-dependent chromosome condensation and heat-stable nucleoid-structuring protein redistribution in *Escherichia coli* under osmotic stress. *J. Bacteriol.*, **201**, e00469-19.
7. Scutigliani,E.M., Scholl,E.R., Grootemaat,A.E., Khanal,S., Kochan,J.A., Krawczyk,P.M., Reits,E.A., Garzan,A., Ngo,H.X., Green,K.D., *et al.* (2018) Interfering with DNA decondensation as a strategy against mycobacteria. *Front. Microbiol.*, **9**, 2034.
8. Gupta,R.S., Lo,B. and Son,J. (2018) Phylogenomics and comparative genomic studies robustly support division of the genus *Mycobacterium* into an emended genus *Mycobacterium* and four novel genera. *Front. Microbiol.*, **9**, 67.
9. World Health Organization (2020) Global Tuberculosis Report 2020. WHO.
10. Matsumoto,S., Yukitake,H., Furugen,M., Matsuo,T., Mineta,T. and Yamada,T. (1999) Identification of a novel DNA-binding protein from *Mycobacteriumbovis* bacillus Calmette-Guérin. *Microbiol. Immunol.*, **43**, 1027–1036.
11. Niki,M., Niki,M., Tateishi,Y., Ozeki,Y., Kirikae,T., Lewin,A., Inoue,Y., Matsumoto,M., Dahl,J.L., Ogura,H., *et al.* (2012) A novel mechanism of growth phase-dependent tolerance to isoniazid in mycobacteria. *J. Biol. Chem.*, **287**, 27743–27752.
12. Matsumoto,S., Furugen,M., Yukitake,H. and Yamada,T. (2000) The gene encoding mycobacterial DNA-binding protein I (MDPI)

transformed rapidly growing bacteria to slowly growing bacteria. *FEMS Microbiol. Lett.*, **182**, 297–301.
13. Rouvière-Yaniv,J. and Gros,F. (1975) Characterization of a novel, low-molecular-weight DNA-binding protein from *Escherichia coli*. *Proc. Natl Acad. Sci. USA*, **72**, 3428–3432.
14. Grove,A. (2011) Functional evolution of bacterial histone-like HU proteins. *Curr. Issues Mol. Biol.*, **13**, 1–12.
15. Swinger,K.K., Lemberg,K.M., Zhang,Y. and Rice,P.A. (2003) Flexible DNA bending in HU–DNA cocrystal structures. *EMBO J.*, **22**, 3749–3760.
16. Ramstein,J., Hervouet,N., Coste,F., Zelwer,C., Oberto,J. and Castaing,B. (2003) Evidence of a thermal unfolding dimeric intermediate for the *Escherichia coli* histone-like HU proteins: thermodynamics and atructure. *J. Mol. Biol.*, **331**, 101–121.
17. Guo,F. and Adhya,S. (2007) Spiral structure of *Escherichia coli* HUalphabeta provides foundation for DNA supercoiling. *Proc. Natl Acad. Sci. USA*, **104**, 4309–4314.
18. Bhowmick,T., Ghosh,S., Dixit,K., Ganesan,V., Ramagopal,U.A., Dey,D., Sarma,S.P., Ramakumar,S. and Nagaraja,V. (2014) Targeting *Mycobacterium tuberculosis* nucleoid-associated protein HU with structure-based inhibitors. *Nat. Commun.*, **5**, 4124.
19. Ohara,Y., Ozeki,Y., Tateishi,Y., Mashima,T., Arisaka,F., Tsunaka,Y., Fujiwara,Y., Nishiyama,A., Yoshida,Y., Kitadokoro,K., *et al.* (2018) Significance of a histone-like protein with its native structure for the diagnosis of asymptomatic tuberculosis. *PLoS One*, **13**, e0204160.
20. Wright,P.E. and Dyson,H.J. (1999) Intrinsically unstructured proteins: re-assessing the protein structure–function paradigm. *J. Mol. Biol.*, **293**, 321–331.
21. Ward,J.J., Sodhi,J.S., Mcguffin,L.J., Buxton,B.F. and Jones,D.T. (2004) Prediction and functional analysis of native disorder in proteins from the three kingdoms of life. *J. Mol. Biol.*, **337**, 635–645.
22. Wright,P.E. and Dyson,H.J. (1999) Intrinsically disordered proteins in cellular signaling and regulation. *J. Mol. Biol.*, **293**, 321–331.
23. Fukuchi,S., Homma,K., Minezaki,Y. and Nishikawa,K. (2006) Intrinsically disordered loops inserted into the structural domains of human proteins. *J. Mol. Biol.*, **355**, 845–857.
24. Wang,C., Uversky,V.N. and Kurgan,L. (2016) Disordered nucleiome: abundance of intrinsic disorder in the DNA- and RNA-binding proteins in 1121 species from Eukaryota, Bacteria and Archaea. *Proteomics*, **16**, 1486–1498.
25. Fukuchi,S., Homma,K., Minezaki,Y., Gojobori,T. and Nishikawa,K. (2009) Development of an accurate classification system of proteins into structured and unstructured regions that uncovers novel structural domains: its application to human transcription factors. *BMC Struct. Biol.*, **9**, 26.
26. Fukuchi,S., Hosoda,K., Homma,K., Gojobori,T. and Nishikawa,K. (2011) Binary classification of protein molecules into intrinsically disordered and ordered segments. *BMC Struct. Biol.*, **11**, 29.
27. Caterino,T.L. and Hayes,J.J. (2011) Structure of the H1 C-terminal domain and function in chromatin condensation. *Biochem. Cell Biol.*, **89**, 35–44.
28. Ando,T. (2018) High-speed atomic force microscopy and its future prospects. *Biophys. Rev.*, **19**, 285–292.
29. Shibata,M., Nishimasu,H., Kodera,N., Hirano,S., Ando,T., Uchihashi,T. and Nureki,O. (2017) Real-space and real-time dynamics of CRISPR-Cas9 visualized by high-speed atomic force microscopy. *Nat. Commun.*, **8**, 1430.
30. Katan,A.J., Vlijm,R., Lusser,A. and Dekker,C. (2015) Dynamics of nucleosomal structures measured by high-speed atomic force microscopy. *Small*, **11**, 976–984.
31. Miyagi,A., Ando,T. and Lyubchenko,Y.L. (2011) Dynamics of nucleosomes assessed with time-lapse high-speed atomic force microscopy. *Biochemistry*, **50**, 7901–7908.
32. Kodera,N., Yamamoto,D., Ishikawa,R. and Ando,T. (2010) Video imaging of walking myosin V by high-speed atomic force microscopy. *Nature*, **468**, 72–76.
33. Kodera,N., Noshiro,D., Dora,S.K., Mori,T., Habchi,J., Blocquel,D., Gruet,A., Dosnon,M., Salladini,E., Bignon,C., *et al.* (2021) Structural and dynamics analysis of intrinsically disordered proteins by high-speed atomic force microscopy. *Nat. Nanotechnol.*, **16**, 181–189.
34. Li,W., Wang,W. and Takada,S. (2014) Energy landscape views for interplays among folding, binding, and allostery of calmodulin domains. *Proc. Natl Acad. Sci. USA*, **111**, 10550–10555.
35. Freeman,G.S., Hinckley,D.M., Lequieu,J.P., Whitmer,J.K. and de Pablo,J.J. (2014) Coarse-grained modeling of DNA curvature. *J. Chem. Phys.*, **141**, 165103.
36. Tan,C., Terakawa,T. and Takada,S. (2016) Dynamic coupling among protein binding, sliding, and DNA bending revealed by molecular dynamics. *J. Am. Chem. Soc.*, **138**, 8512–8522.
37. Wu,H., Dalal,Y. and Papoian,G.A. (2021) Binding dynamics of disordered linker histone H1 with a nucleosomal particle. *J. Mol. Biol.*, **433**, 166881.
38. Whiteford,D.C., Klingelhoets,J.J., Bambenek,M.H. and Dahl,J.L. (2011) Deletion of the histone-like protein (Hlp) from *Mycobacterium smegmatis* results in increased sensitivity to UV exposure, freezing and isoniazid. *Microbiology*, **157**, 327–335.
39. Matsumoto,S., Tamaki,M., Yukitake,H., Matsuo,T., Naito,M., Teraoka,H. and Yamada,T. (1996) A stable *Escherichia coli*–mycobacteria shuttle vector 'pSO246' in *Mycobacterium bovis* BCG. *FEMS Microbiol. Lett.*, **135**, 237–243.
40. Dame,R.T. and Goosen,N. (2002) HU: promoting or counteracting DNA compaction?*FEBS Lett.*, **529**, 151–156.
41. Japaridze,A., Muskhelishvili,G., Benedetti,F., Gavriilidou,A.F.M., Zenobi,R., De Los Rios,P., Longo,G. and Dietler,G. (2017) Hyperplectonemes: a higher order compact and dynamic DNA self-organization. *Nano Lett.*, **17**, 1938–1948.
42. Van Noort,J., Verbrugge,S., Goosen,N., Dekker,C. and Dame,R.T. (2004) Dual architectural roles of HU: formation of flexible hinges and rigid filaments. *Proc. Natl Acad. Sci. USA*, **101**, 6969–6974.
43. Dame,R.T., Wyman,C. and Goosen,N. (2000) H-NS mediated compaction of DNA visualised by atomic force microscopy. *Nucleic Acids Res.*, **28**, 3504–3510.
44. Mukherjee,A., Bhattacharyya,G. and Grove,A. (2008) The C-terminal domain of HU-related histone-like protein Hlp from *Mycobacterium smegmatis* mediates DNA end-joining. *Biochemistry*, **47**, 8744–8753.
45. Sharadamma,N., Khan,K., Kumar,S., Neelakanteshwar Patil,K., Hasnain,S.E. and Muniyappa,K. (2011) Synergy between the N-terminal and C-terminal domains of *Mycobacterium tuberculosis* HupB is essential for high-affinity binding, DNA supercoiling and inhibition of RecA-promoted strand exchange. *FEBS J.*, **278**, 3447–3462.
46. Dai,L., Mu,Y., Nordenskiöld,L. and van der Maarel,J.R. (2008) Molecular dynamics simulation of multivalent-ion mediated attraction between DNA molecules. *Phys. Rev. Lett.*, **100**, 118301.
47. Turner,A.L., Watson,M., Wilkins,O.G., Cato,L., Travers,A., Thomas,J.O. and Stott,K. (2018) Highly disordered histone H1–DNA model complexes and their condensates. *Proc. Natl Acad. Sci. USA*, **115**, 11964–11969.
48. Sridhar,A., Farr,S.E., Portella,G., Schlick,T., Orozco,M. and Collepardo-Guevara,R. (2020) Emergence of chromatin hierarchical loops from protein disorder and nucleosome asymmetry. *Proc. Natl Acad. Sci. USA*, **117**, 7216–7224.
49. Arold,S.T., Leonard,P.G., Parkinson,G.N. and Ladbury,J.E. (2010) H-NS forms a superhelical protein scaffold for DNA condensation. *Proc. Natl Acad. Sci. USA*, **107**, 15728–15732.
50. McGovern,V., Higgins,N.P., Chiz,R.S. and Jaworski,A. (1994) H-NS over-expression induces an artificial stationary phase by silencing global transcription. *Biochimie*, **76**, 1019–1029.
51. Enany,S., Yoshida,Y., Tateishi,Y., Ozeki,Y., Nishiyama,A., Savitskaya,A., Yamaguchi,T., Ohara,Y., Yamamoto,T., Ato,M., *et al.* (2017) Mycobacterial DNA-binding protein 1 is critical for long term survival of *Mycobacterium smegmatis* and simultaneously coordinates cellular functions. *Sci. Rep.*, **7**, 6810.

52. Shaban,A.K., Gebretsadik,G., Hakamata,M., Takihara,H., Inouchi,E., Nishiyama,A., Ozeki,Y., Tateishi,Y., Nishiuchi,Y., Yamaguchi,T., *et al.* (2023) Mycobacterial DNA-binding protein 1 is critical for BCG survival in stressful environments and simultaneously regulates gene expression. *Sci. Rep.*, **13**, 14157.
53. Jiang,K., Zhang,C., Guttula,D., Liu,F., van Kan,J.A., Lavelle,C., Kubiak,K., Malabirade,A., Lapp,A., Arluison,V., *et al.* (2015) Effects of Hfq on the conformation and compaction of DNA. *Nucleic Acids Res.*, **43**, 4332–4341.
54. Malabirade,A., Jiang,K., Kubiak,K., Diaz-Mendoza,A., Liu,F., van Kan,J.A., Berret,J.F., Arluison,V. and van der Maarel,J.R.C. (2017) Compaction and condensation of DNA mediated by the C-terminal domain of Hfq. *Nucleic Acids Res.*, **45**, 7299–7308.
55. Ragonis-Bachar,P. and Landau,M. (2021) Functional and pathological amyloid structures in the eyes of 2020 cryo-EM. *Curr. Opin. Struct. Biol.*, **68**, 184–193.
56. Turbant,F., Hamoui,O.E., Partouche,D., Sandt,C., Busi,F., Wien,F. and Arluison,V. (2021) Identification and characterization of the Hfq bacterial amyloid region DNA interactions. *BBA Adv.*, **1**, 100029.
57. Griffin,J.E., Gawronski,J.D., Dejesus,M.A., Ioerger,T.R., Akerley,B.J. and Sassetti,C.M. (2011) High-resolution phenotypic profiling defines genes essential for mycobacterial growth and cholesterol catabolism. *PLoS Pathog.*, **7**, e1002251.

Received: March 8, 2023. **Revised:** October 17, 2023. **Editorial Decision:** November 13, 2023. **Accepted:** November 23, 2023